Environmental Science and Pollution Research (2024) 31:15322–15338
https://doi.org/10.1007/s11356-024-32195-3

RESEARCH ARTICLE

Optimizing slug bubble size for application of the ultra-thin flat sheet membranes in MBR: a comprehensive study combining CFD simulation and experiment

Xinyue Wu[1,2] · Lian Yang[1,2] · Jiang Chang[2] · Shuoxun Dong[1] · Feng Xiao[1]

Received: 16 August 2023 / Accepted: 21 January 2024 / Published online: 31 January 2024

Abstract

Optimizing the slug bubble size specifically for ultra-thin flat sheet membranes in MBR systems can effectively enhance the scouring force and improve fouling control efficiency, thereby further advancing their targeted and widespread application. In this study, a three-dimensional model was developed based on the practical application to investigate the impact of slug bubbles on scouring performance in ultra-thin flat sheet MBR systems, encompassing their evolution, disturbance level, and shear stress. A membrane fouling probability index for quantifying the distribution of membrane fouling, along with a turbulence intensity index have been proposed. The findings revealed that the 20-mL slug bubble induced the highest disturbance level in the surrounding fluid, characterized by an instantaneous peak velocity of 0.63 m/s at the local system level, conducive to bubble scouring. And exerted the greatest shear stress effect, achieving the most effective reduction in membrane contamination, with a maximum shear stress of 1.82 Pa. The experimental validation conducted during the operational cycles confirmed that the scouring effect of 20-mL slug flow yielded in a maximum proportion of 48.16% within the low fouling probability region. The results provided evidence supporting the assertion that specific aeration conditions producing 20 mL of bubbles resulted in minimal membrane fouling, ensuring a more pronounced scouring effect. The combination anythsis of slug bubble characteristics and behaviors, integrating theoretical and experimental approaches, implied that 20 mL was the optimal bubble size in ultra-thin flat sheet MBR, which fulfilled the optimal air scouring effect.

Keywords Volume-of-fluid method · Slug bubble · Vortex · Shear stress · Flat sheet membranes · Bubble disturbance

Introduction

The membrane bioreactor (MBR) is extensively employed to treat and recycle industrial and municipal wastewater, which combines membrane separation technology with the activated sludge method (Meng et al. 2017; Xiao et al. 2019). The development of strategies to control membrane surface fouling is necessary in actual applications to maintain permeability and overall treatment plant capacity (Wang et al. 2018, 2022, 2021). The structure of membrane elements and aeration parameter optimization were regarded as effective strategies for membrane fouling control due to its operability and accessibility (Du et al. 2017; Ghosh and Cui 1999; Golrokh Sani et al. 2021).

The uniform scour achieved through aeration in flat sheet membranes significantly reduces backflushing rates, resulting in remarkable anti-fouling properties and effective pollutant cut-off (Hashisho et al. 2016). The traditional flat sheet membranes in practical MBR applications typically use acrylonitrile–butadiene–styrene (ABS) copolymer plates as the membrane inner chamber support layer (He et al. 2020; Liu et al. 2018). Flat sheet membrane elements mostly encounter issues such as expansive surface area, restricted water channels on the support layer, and an impractical structure, leading to low packing density, reduced water production rates, sludge cake accumulation, and higher operating costs for flat sheet membrane bioreactors (FMBRs). In comparison, the ultra-thin flat membranes proposed by the Beijing Drainage Group Co. Ltd. have optimized the

Responsible Editor: Angeles Blanco

✉ Feng Xiao
xiaofeng@ncepu.edu.cn; fengxiao@rcees.ac.cn

[1] School of Water Resources and Hydropower Engineering, North China Electric Power University, Beijing 102206, China

[2] Beijing Drainage Group Co. Ltd, Beijing 100044, China

original properties of traditional flat membranes, effectively improved operational efficiency and further reducing membrane fouling. The membranes with gridded water channels replace conventional ABS sheets, resulting in the reduction of filtration resistance, a reduction in thickness from 5 to 7 mm to 1.2 mm and a packing density of from 55 up to 90 $m^2 \cdot m^{-3}$. These qualities render MBR operation cost-effective, promote efficient backwashing, and induce membrane jittering to enhance disturbance in the surrounding fluid under aeration conditions. However, excessively small bubble sizes may lead to inadequate scouring, while overly large sizes increase aeration energy consumption (Ndinisa et al. 2006; Zhang et al. 2019). The high packing density of ultra-thin flat membranes emphasizes the need to optimize bubble size and scouring effects for effective membrane fouling control in MBR applications.

The bubble size is a critical factor in the aeration parameter optimization that determines the efficiency of fouling control in aeration systems, and slug bubbling has been recognized as a viable approach for mitigating fouling in FSMBRs. The CFD simulation method has proven to be a powerful tool for comprehensively and quantitatively characterizing the flow field characteristics of MBR method, providing data support to address optimize the bubble size (Liu et al. 2018). Radaei et al. (2018) investigated the hydrodynamic characteristics of sizable spherical cap bubbles, ranging in size from 58 to 290 mL. Wei et al. (2013) studied the wall shear stress with slug bubbles of sizes ranging from 5 to 200 mL. However, the research on optimizing bubble size mostly used shear stress as the sole criterion to determine the scouring effect of bubbles. The scouring effect of the corresponding bubble is strongly related to its shape, wake, and the disturbance level to the surrounding fluid (Gumulya et al. 2021; Liu et al. 2019; Wang and Brito-Parada 2021). There are studies indicating that neglecting the behavior of bubbles in simulations can lead to inaccurate calculation of shear stress (Ratkovich et al. 2009). Therefore, the detailed fluid dynamic characteristics of the entire membrane surface generated by bubbles in ultra-thin flat sheet MBRs are still unclear, and further optimization of slug bubble size is required to achieve a better scouring effect. The integration of comprehensive experimental studies with localized simulations yields realistic and reliable results. As a result, the study was undertaken to provide more effective guidance for the extensive practical use of ultra-thin flat sheet membranes, employing a synergistic approach that combines theory and experimentation.

In this study, a three-dimensional CFD model was developed based on a practical application of MBR system to simulate the rising process of different-sized slug bubbles between two local ultra-thin flat-sheet membrane modules, ranging from 5 to 29 mL. The system, designed for domestic wastewater treatment and reclamation, has a daily processing capacity of 40,000 m^3/d and is situated in Beijing, China. The study proposed a membrane fouling probability index for quantifying the distribution of membrane fouling, along with a turbulence intensity index. This was accompanied by quantitative analysis of the characteristics and scouring effects of the bubbles, including their evolution, disturbance level, and shear stress. Furthermore, by combining experimental verification of the terminal velocity of bubbles and membrane fouling extent, a comprehensive analysis of the scouring effect of the slug bubbles on the membrane surface was conducted. Finally, the optimal bubble parameters that produced the most substantial scouring effect during the practical operation of the ultra-thin membrane MBR were determined, and the corresponding mechanisms were subsequently investigated. The implementation of this optimization study would facilitate the further widespread application of ultra-thin flat membranes.

Material and methods

Operation and equipment setup

The study utilized an ultra-thin flat membrane module (Beijing Drainage Group Co. Ltd., China) as the research subject. The experiment was conducted on a pilot-scale membrane pool (Fig. 1a) with dimensions of 500 mm × 500 mm × 700 mm (length × width × height). The membrane pool was equipped with 64 ultra-thin flat-sheet membrane elements arranged from outer to inner, with each membrane measuring 500 mm × 500 mm and channel gap of 7 mm. The experimental arrangement comprised an air compressor and a buffer tank, wherein the buffer tank served as a damper to eliminate flow pulsations. The flow rate was regulated by utilizing a pressure regulator while maintaining a constant pressure. Upon opening the solenoid valve, air entered the tank, leading to the formation of bubbles. The horizontal aeration tube, consisting of a single perforated pipe with a diameter of 32 mm and featuring ten orifices, each with a diameter of 5 mm, injects aeration into the tank. The formed bubbles made contact with the flat sheet membranes and ascended at the outlet position. The aeration pipe was horizontally positioned because when the air was horizontally injected, bubbles quickly formed within the valve opening time and then started to ascend. When the pipe was vertically upwardly injected with air, it resulted in a cluster of rapidly ascending jet bubbles rather than individual bubbles as shown in Fig. 1b. The bubble frequency ranged from 1 to 0.2 Hz, with the closing and opening time of the valve controlled by a timer, ensuring a minimum time interval of 10 ms. The time was determined through repeated experiments to ensure a constant pressure and flow rate, minimizing any noticeable fluctuations. The air in the

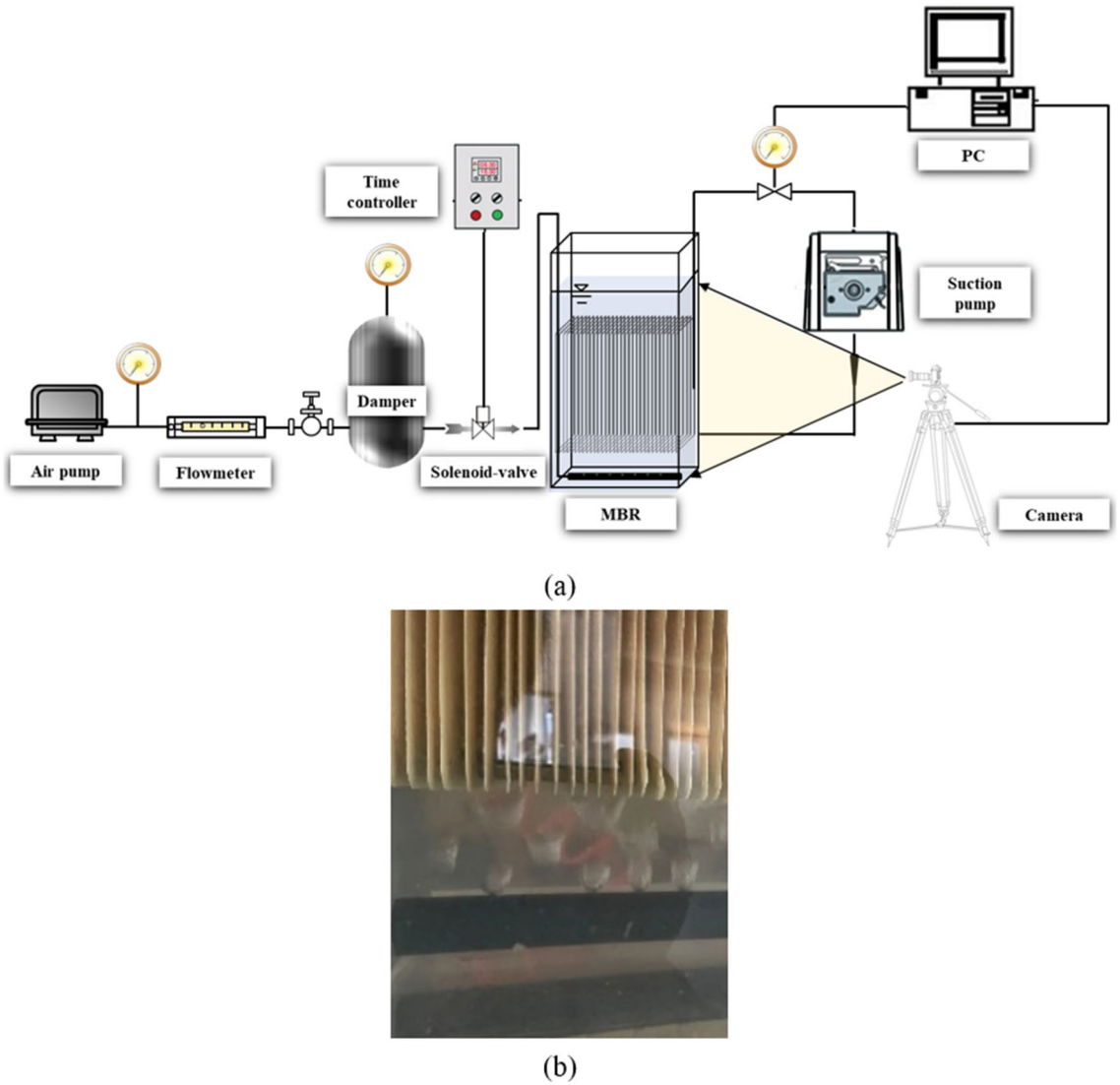

Fig. 1 **a** Scheme of the experimental MBR process and **b** picture of the aeration process

pipe was flushed by continuous air injection twice before the start of the experiment. The air in the pipe was released to stabilize the pressure and flow rate in the damper. After the flow pulsations were eradicated (after scouring), a steady air pressure was maintained behind the solenoid valve, resulting in uniform bubble volumes during each opening period. This facilitated the calculation of bubble volume by dividing the air velocity by the frequency, following the method described by Zhang et al. (Zhang et al. 2009).

The peristaltic pump was connected to the ultra-thin flat sheet membrane module, operating in a mode of 8 min of water production followed by 2 min (Wang et al. 2014) of rest, during filtration, with a constant permeate flux of 18 LMH (L/m^2/h) was monitored. The influent water, derived from urban domestic wastewater, maintained a temperature of 20 °C and was characterized by a COD of 214.59 mg/L, turbidity of 77.00 mg/L, and suspended solid concentration of 123.26 mg/L. The variation of transmembrane pressure (TMP) over time was monitored throughout a 7-day (Wang et al. 2014) operating cycle, under different aeration conditions with varying sizes of slug bubbles.

CFD simulation

Physical model and meshing

A three-dimensional model of the membrane module, which utilizes the ultra-thin flat sheet membrane from the Beijing Drainage Group, was set up using ANSYS FLUENT 19.2 to investigate the optimal size of slug bubbles in the bioreactor. The model captured the movement and evolution of individual bubbles while taking into account the interaction

Table 1 Details of CFD model setup

Domain size	Membrane elements size	Spacing	Primary phase	Secondary phase
500×700×9.4 mm	500×500×1.2 mm	7.0 mm	Mixture with a viscosity of 1.96×10^{-3} Pa·s	Air

Table 2 Characteristics of ultra-thin flat sheet membrane

Membrane type	Packing density ($m^2 \cdot m^{-3}$)	Operating cost	Single sheet thickness (mm)	Backwashing
Ultra-thin flat sheet membrane	90	Low	1.2	Jitter during the backwashing process

between height and bubbles. To determine the hydrodynamic properties within the flat sheet module as well as throughout the full flat sheet membrane surface, the domain design was consistent with the local membrane module as shown in Fig.S1. Details of CFD model setup were presented in Table 1. The main component of the model consists of two ultra-thin flat sheet membrane elements. The membranes exhibit certain advantageous characteristics (Table 2). The top of the computational domain configured as an outflow boundary. The bubbles of different sizes were introduced as patches with corresponding initial velocities, contributing to the development of a turbulent flow state. The model involved the release of individual spherical bubbles from the center of the membrane channel at the bottom of the membrane, within a mixture system where the viscosity aligned with that of sludge at 8000 mg/L. The initial bubble size was set as 5 mL, 10 mL, 15 mL, 20 mL, 25 mL, or 29 mL, respectively, to study the corresponding hydrodynamic effect. This range was determined by combining the actual operating characteristics of the MBR with phase diagrams on the Galileo-Eoctua plane that depict five distinct regimes with distinct boundaries (Tripathi et al. 2015).

The symmetrical boundary method was used to reduce the calculation amount and improve the calculation accuracy. The grid distribution of the refined region close to the membrane surface was separated into various sub-layers in order to explore more precisely the properties of the flow field and shear stress in the vicinity of the membrane (Fig. S1b left). To improve the local resolution of gas–liquid interface capture, the membrane module and the following areas had increased grid density and further densified the rising area of the slug bubbles for the set bubble sizes (Fig. S1b right). The mesh contained 821,762 cells, 679,220 faces, and 751,032 nodes. The mesh independence test was conducted by varying the number of maximum inflation layers, leading to an increase in the corresponding grid count from 6.1×10^5 to 12.4×10^5. Table. 3 gives details for the results of meshing. The maximum difference in the simulated mean flow velocity and shear force obtained between the number of boundary layers 5 and 9 was 4.8% and 3.4%, respectively, as shown in Fig. S2.

Table 3 The results of meshing with different number of boundary layers

Maximum layers of inflation	Nodes	Elements	Mesh quality
3	604,885	610,644	0.99516
5	751,032	821,762	0.99742
7	897,178	1,032,879	0.98625
9	1,043,325	1,243,996	0.97984

Therefore, a grid of 8.2×10^5 elements under the corresponding 5 boundary layer to 12.4×10^5 under the corresponding 9 boundary layer can be considered as grid-independent, and the final grid of 5 boundary layers was chosen because the parameters simulated were all within 5% compared to the grid using the highest number of layers. In addition, the EquiSize Skew parameter values were between 0 and 0.4 accounts (0 to best; 1-worst) for 99.74% of all computational domains by detecting mesh quality. The high-quality grids directly affected the simulation time and convergence stability.

Governing equations

The volume of fluid (VOF) model was used to forecast the formation of large bubbles with the resolution of the gas–liquid interface tracking problem, which could track and identify the trailing vortex/deformation of bubbles and the interaction between them (Ngo et al. 2023). The simulation was done by calculating the mass and momentum conservation, pulsing equations for turbulence and the tracking of the interface (Hirt and Nichols 1981). The governing equation is the equation for the conservation of continuity equation, for incompressible two-phase flow, which is represented as Eq. (1),

$$\frac{\partial \rho}{\partial t} + \nabla\left(\rho\vec{u}\right) = 0 \tag{1}$$

and the momentum equation was Eq. (2)

$$\frac{\partial}{\partial t}\left(\rho\vec{u}\right) + \nabla\left(\rho\vec{u}\vec{u}\right) = -\nabla P + \rho\vec{g} + \vec{F} + \nabla\vec{\tau} \tag{2}$$

where $\vec{P}$, $\vec{g}$, and $\vec{F}$ are, respectively, the pressure, gravitational acceleration, and volumetric surface tension force, respectively. The properties observed in the transport equation were determined by the presence of constituent phases in each control volume. The density ρ and viscosity μ depend on the volume fraction α occupied by q th phases, which are employed as

$$\rho = \sum \alpha_q \rho_q \tag{3}$$

$$\mu = \sum \alpha_q \mu_q \tag{4}$$

The advection term of the VOF model made use of the piecewise-linear interface calculation (PLIC) methodology, which allowed for more precise tracking of the interface between the fluids. The approach involves constructing the fluid interface geometrically. The d parameter is defined using the volume fraction and the normal orientation m, according to

$$m = \nabla \alpha \tag{5}$$

$$m_x x + m_y y + m_z z = d \tag{6}$$

A front-tracking method is employed to simulate turbulent flow in a vertical channel with deformable bubbles (Feng et al. 2019). Simulation of turbulence effect caused by aeration using a realizable k-ε model (Shih et al. 1995). The kinetic energy of the turbulence is denoted by k in this model, while the dissipation rate is denoted by ε. As a result, Eqs. (7) and (8) are additional transport equations

$$\frac{\partial}{\partial_t}(\rho k) + \frac{\partial}{\partial x_j}\left(\rho k \overline{u_j}\right) = \frac{\partial}{\partial x_j}\left[\left(\mu + \frac{\mu_t}{\sigma_k}\right)\frac{\partial k}{\partial x_j}\right] + G_\kappa + G_b - \rho\varepsilon - Y_M \tag{7}$$

$$\frac{\partial}{\partial_t}(\rho k) + \frac{\partial}{\partial x_j}\left(\rho k \overline{u_j}\right) = \frac{\partial}{\partial x_j}\left[\left(\mu + \frac{\mu_t}{\sigma_\varepsilon}\right)\frac{\partial k}{\partial x_j}\right] + \rho C_1 S\varepsilon - \rho C_2 \frac{\varepsilon^2}{k + \sqrt{v\varepsilon}} + C_{1\varepsilon}\frac{\varepsilon}{k} C_{3\varepsilon} G_b + S_\varepsilon \tag{8}$$

where

$$\mu_t = C_\mu \rho \frac{k^2}{\varepsilon}$$

$$C_1 = \max\left[0.43, \frac{\eta}{\eta + 5}\right]$$

$$\eta = S\frac{k}{\varepsilon}$$

$$S = \sqrt{2S_{ij}S_{ij}}$$

In which, G_k indicates the generation of turbulent kinetic energy due to average velocity gradients, G_b is the kinetic energy from turbulence caused by buoyancy. C_μ is a function of the rotation, mean strain, and turbulence fields. Y_M represents the contribution of compressible turbulent pulsating expansion to the overall dissipation rate. The turbulent Prandtl number σ_k and σ_ε were 1.0 and 1.2, respectively. S_k and S_ε are user-defined source terms. C_2, $C_{1\varepsilon}$, and $C_{3\varepsilon}$ are constants (Brackbill et al. 1992).

The continuous surface force (CSF) model was used to determine surface tension at an interface (Brackbill et al. 1992). As a volume force, the surface tension $\underset{F\ vol}{\rightarrow}$ can be described as follows

$$\rho_L - \rho_G = \sigma k \tag{9}$$

$$\underset{F\ vol}{\rightarrow} = \sigma \frac{2\rho\kappa\nabla_{\alpha G}}{\left(\rho_L + \rho_G\right)} \tag{10}$$

where κ is the divergence of the unit normal describing the surface curvature:

$$\kappa = \nabla \frac{n}{|n|}$$

$$n = \nabla \alpha_G$$

Numerical methods and boundary conditions

To effectively depict the bubble movement through the membrane module channel, a 3D simulation was selected. The unsteady scheme was solved by the implicit time-marching scheme of the first order. The model used a continuous phase for the liquid and the physical characteristics of air was utilized for the dispersed gas phase, with the following assumptions on isothermal properties: 1) bubbles released from the bottom of the membrane were initialized as spherical shapes, considering the efficient acquisition of fluid and bubble behavioral trends; 2) the initial release velocity of the bubbles was set to correspond to the sizes shown in Table 4. based on the aeration conditions that generate bubbles of different sizes; and 3) no bubble collisions, coalescence or break-ups. The PLIC scheme (Youngs 1982) was chosen to interpolate the gas–liquid interface.

The simulation was carried out on the pressure-based solver, and the momentum and k-ε equations were discretized into the second-order upwind scheme. Pressure–velocity coupling using PISO (pressure implicit operator splitting) and PRESTO! (pressure oscillation option) solutions discretized the pressure terms. The bottom of the model was set to velocity inlet with the liquid velocity of

Table 4 The initial velocities corresponding to the bubbles with different sizes

Bubble size (mL)	5	10	15	20	25	29
Initial velocity (m/s)	0.4345	0.2173	0.1448	0.1086	0.0869	0.0724

zero, while the condition at the outlet was outflow. There was no fluid-slip situation on the membrane surface, and all other boundaries were stationary. The membrane walls were presumed to be impermeable, as the permeate rate is typically below 0.5% of the total cross-flow velocity in the channel under industrial membrane processes (Du et al. 2017). In addition, the flow field was not distorted by the wall suction (Kaya et al. 2014). Since the Courant number was maintained below 0.25, the time step was set at approximately 10^{-4} s. The simulation lasted about 1.0 s before the bubble reached a steady state. By stable, we meant that they had not undergone central fragmentation, not that their shape had remained constant.

Analysis methods

Bubble characteristics

The factors such as the properties of the liquid and bubble size influence the characteristics and behaviors of bubble flow, including the shape and velocity of bubbles(Zhang et al. 2021). Three important dimensionless numbers, namely, Morton Eq. (17), Eotvos Eq. (18), and Reynolds Eq. (19), quantify the physical properties of the phases, as well as the shape and motion characteristics of bubbles (Clift et al. 1978). Morton number describes the relative effect of surface tension and inertia. Eotvos number considers the density difference between the bubble and the surrounding medium, as well as the relationship with surface tension, and together with the Morton number, it represents the shape and trajectory of the bubble. Reynolds number represents the ratio of inertia to viscosity.

$$R_e = \frac{\rho_l U d_e}{\mu_l} \tag{11}$$

$$M_o = \frac{g\mu_l{}^4\left(\rho_l - \rho_g\right)}{\rho_l{}^2\sigma^3} \tag{13}$$

$$E_o = \frac{g\left(\rho_l - \rho_g\right)d_e{}^2}{\sigma} \tag{14}$$

In which, g represents gravity (m/s^2) and d_e stands for the equivalent spherical diameter of the bubble (m) calculated using Eq. (20). The variables ρ_l (kg/m^3), μ_l (kg/(m-s)), σ (N/m), ρ_g (kg/m^3), and U (m/s) denote the density, viscosity of the liquid, surface tension, density of the gas, and bubble terminal rise velocity, respectively.

$$d_e = \sqrt[3]{\frac{6V}{\pi}} \tag{15}$$

where V is the bubble volume (m^3).

Vortex identification method

Vortex identification was conducted to analyze the wake vortex. The maximum vorticity threshold or iso-surfaces of vorticity could be used to display these structures using the vorticity magnitude. To better identify the vortex structure digitally, as one of the standard methods of vortex visualization, the Q criterion not only has high computational efficiency but also can directly reflect the dominant factor of vortex intensity (Gao et al. 2019).

The value Q is derived from the definition of the velocity gradient tensor, which is written as $\frac{\partial u_i}{\partial x_j}$, in tensor notation. This definition may be decomposed into two pieces, which are as follows

$$\frac{\partial u_i}{\partial x_j} = 0.5 \times \left[\frac{\partial u_i}{\partial x_j} + \frac{\partial u_j}{\partial x_i}\right] + 0.5 \times \left[\frac{\partial u_i}{\partial x_j} - \frac{\partial u_j}{\partial x_i}\right] \tag{16}$$

where S denotes the symmetric portion and is known as the strain rate tensor defined by

$$S = 0.5 \times \left[\frac{\partial u_i}{\partial x_j} + \frac{\partial u_j}{\partial x_i}\right] \tag{17}$$

and the antisymmetric component denoted as Ω is the rotation rate or vorticity tensor, as described by

$$\Omega = 0.5 \times \left[\frac{\partial u_i}{\partial x_j} - \frac{\partial u_j}{\partial x_i}\right] \tag{18}$$

The second invariant of the velocity gradient tensor is thus defined as Q:

$$Q = 0.5 \times \left[\|\Omega\|_F^2 - \|S\|_F^2\right] \tag{19}$$

The regions with positive values of Q demonstrate the existence of vortexes (Zhan et al. 2019), which indicate regions of the flow field where vorticity dominates, whereas negative values of Q denote regions where strain rate or viscous stress dominate. Therefore, the index V_S measuring the vortex strength and the disturbance level was proposed by

$$V_S = \frac{\left|Q_p\right|}{\left|Q_n\right|} \tag{20}$$

where Q_p is the sum of positive Q values and Q_n is the sum of negative Q values. A higher value of this index indicates a greater level of disturbance generated.

Probability of membrane fouling

The probability of membrane fouling refers to the likelihood of interactions between pollutants or particles and the membrane surface during membrane separation, resulting in membrane surface contamination. The membrane fouling probability index for quantifying the distribution of membrane fouling is employed to assess the likelihood of membrane fouling and offers guidance for optimizing operational strategies. The analysis focused on the distribution of shear forces on the membrane surface to calculate the probability of particle deposition. This study examined the forces acting on micrometer scale particles, considering the particle size that contributes to membrane fouling during the actual operation of an MBR. The resistance offered by the permeate flow drives particles toward the membrane surface. Equation (16) reveals that the forces responsible for particle detachment from the membrane surface primarily include Brownian diffusion forces, influencing smaller colloidal particles, as well as shear-induced diffusion forces (Kovalchuk et al. 2008) and inertial lift forces (Liu et al. 2017), affecting larger particles. The corresponding fluxes are J_B, J_S, and J_I. When the forces facilitating particle migration to the membrane surface are in equilibrium with the forces causing particle detachment, a critical state, known as the critical flux J_c, is attained (Lan et al. 2017). At this critical state, membrane surface deposition is effectively avoided. The migration mechanism of submicron particles with diameters smaller than 1 µm, primarily governed by Brownian diffusion forces, is involved in the process of particle diffusion and deposition.

$$J_c = J_{tot} = J_B + J_S + J_I \tag{21}$$

$$J_B = 0.185\left(\frac{\gamma_w \kappa^2 T^2 \phi_w}{\eta_f^2 \alpha^2 L \phi_b}\right)^{1/3} \tag{22}$$

$$J_S = 0.072\gamma_w\left(\frac{\alpha^4 \phi_w}{L\phi_b}\right)^{1/2} \tag{23}$$

$$J_I = 0.036\frac{\rho_f \alpha^3 \gamma_w^2}{\eta_f} \tag{24}$$

In the given equation, γ_w quantifies the velocity at which adjacent layers of the fluid move concerning one another. The Boltzmann constant (κ) is a fundamental constant in physics that links temperature to the average kinetic energy of particles. The absolute temperature (T) represents the overall thermal energy within the system. η_f measures the resistance of the fluid to flow. The particle diameter (α) provides information about the size of the particles involved. L is the membrane length that specifies the spatial extent of the membrane. The density (ρ_f) quantifies the mass per unit volume of the fluid. The volume fractions of particles at the edge of the filter cake (ϕ_w) and in the suspension (ϕ_b) reflect the relative amounts of particles present in these respective regions. The concentration polarization factor represents the ratio between these volume fractions and captures the degree of concentration polarization occurring in the system.

The relationship between the actual membrane flux J and the critical flux J_c (Liu et al. 2023) is used to determine the probability of membrane fouling (Eq. (20)).

$$E = \frac{J}{J + J_c} \tag{25}$$

When $J < J_c$, the probability of particle deposition is low. Conversely, particles are more likely to deposit under the influence of permeation drag force. According to Eq. (20), $E = 0.5$ represents the critical value, and when $E < 0.5$, a smaller E value indicates a lower likelihood of membrane fouling.

Experiment proof

Fouling assessment

The trans-membrane pressure (TMP) was regularly monitored using a manometer and recorded at 20-s intervals by a paperless recorder. The highest TMP value within each "8-min-on" period was chosen to indicate the instantaneous fouling level and was utilized to construct the TMP profile over the course of long-term operation. In each fouling test, a new membrane module after chemical cleaning was used. The chemical cleaning was performed approximately every seven days or when the trans-membrane pressure (TMP) reached around − 30 kPa. During the cleaning process, the peristaltic pump was employed to draw 1500 mg/L sodium hypochlorite solution into the membrane tank. After allowing it to stand for 2–3 h, the system underwent a 1-h air scouring period by opening the pump valve. Filtration of deionized water was initially conducted for 30 min to build up a steady flow field. Once the steady state with respect to TMP was attained, the feed was switched to the suspension to initiate the fouling test.

Scanning electron microscopy (SEM)

The examination of fouled membrane surfaces involved a meticulous analysis utilizing advanced imaging techniques. A ZEISS field emission scanning electron microscope (SEM, Zeiss Merlin Compact, Germany) was operated at 10.0 kV to ensure high-resolution imaging capabilities. This SEM facilitated a detailed exploration of surface characteristics, offering insights into the intricate structures and features associated with membrane fouling. The membrane, trimmed to dimensions of 5 mm × 5 mm, underwent a 1-min gold-sputtering process before being subjected to SEM measurements. The analysis encompassed a comprehensive exploration of the microstructure of the membrane, providing valuable information crucial for understanding the mechanisms of fouling and enhancing the robustness of our findings.

Terminal velocity

A sophisticated high-speed camera was employed to capture the dynamic journey of bubbles in great detail. The motion of bubbles within the tank, from their inception to reaching the top, was captured through images taken by the camera. The initial ascending velocity of bubbles with different sizes and frequencies was determined by observing the bubble flow near the air inlet. The digital of camera shutter speed was set to 1/10 s to ensure clear and non-blurred images. Subsequently, the recorded images were analyzed using ImageJ software to calculate the terminal velocity of the bubbles by measuring the displacement of the bubble nose over the recorded time frames. The methodological approach not only provided accurate insights into the dynamic behavior of bubbles but also ensured the reliability and precision of the obtained results.

Results and discussions

Model validation

The numerical simulation results of the final stable shape of the bubble were compared with the well-known Clift's graphical correlation (Clift et al. 1978; Grace 1973, 1983; Grace et al. 1976), seeking to verify the accuracy of the numerical method employed in this paper.

The rising bubble behaviors with the initial size of 5 mL, 10 mL, 15 mL, 20 mL, and 29 mL in the liquid have been simulated. The Morton, Eotvos, and Reynolds numbers for bubbles of varying sizes, calculated based on the physical properties of the phase, are presented in Table 5. The final stable shape, obtained through numerical methods following the prescribed approach, were also summarized.

The stable bubble shapes in this study were spherical caps in post-processing by extraction. The steady-state bubble shape points corresponding to different initial bubble sizes in combination with the bubble characteristic index are located in the corresponding regions according to the bubble characteristic map (Fig. S3) developed by Clift et al. The calculating final stable shapes were in good agreement with the results from the graphical correlation for these cases. Consequently, the CFD model developed demonstrated a

Table 5 Steady rising parameters of slug bubbles with different sizes

V (mL)	M_o	E_o	R_e	Numerical stable shape
5	2.61×10^{-11}	63.72	6839.04	
10	2.61×10^{-11}	96.39	8471.86	
15	2.61×10^{-11}	126.31	8645.57	
20	2.61×10^{-11}	153.01	9078.08	
25	2.61×10^{-11}	177.55	9292.56	
29	2.61×10^{-11}	196.01	9470.59	

reliable simulation of the hydrodynamic field generated by slug bubbles in the ultra-thin flat sheet MBR system.

Bubble evolution

Bubble projections were chosen as the subject of study for the purpose of facilitating the observation of bubble evolution. Figure 2 presented the slug bubbles of different sizes moved upwards and reached a steady state with no central fragmentation from 0.0 to 1.0 s. The deformation of upfloated bubbles could potentially predispose a significant "hydrodynamic effect" to alleviate the fouling between the membranes. The distribution of smaller satellite bubbles trailing the primary bubble exhibited a clearly linear pattern. The obtained results unveiled a three-stage process in the evolution of the rising bubbles. As the first step, a depression appeared at the trailing edge and its development caused the spontaneous liquid jet as the bubbles rose. The fluid encountered blockage near the lower edge of the bubbles during fluctuations in flow rate and pressure due to the liquid flowing around the bubbles. In the second stage, the jet lengthened to a certain time and turned to the width direction to form the earlobe shape. Finally, the liquid truncated the bubble and new bubbles were generated when the capillary pressure in the channel decreased to a critical value. The emergence of these small bubble groups could be inferred to enhance the scouring effect of bubbles on the membrane surface. The results also confirmed that the intermittently injected slug bubbles rose along the central line.

The simulation results also showed that the wake region of bubbles generated through necking gradually expanded as the bubble size increased. The bubbles appeared asymmetric phenomenon at nearly 1.0 s after the bubble size reached 20 mL, obviously. The alteration could potentially affect the acceleration of surrounding fluid disturbances caused by the bubble evolution, and the resulting hydrodynamic effects were beneficial to hinder the membrane fouling.

Disturbance level of bubbles

Velocity distribution

The motion of bubbles produced strong disturbances to the surrounding fluid and the velocity distribution could intuitively reflect the flow characteristics during the evolution process. The details are in Fig. S4a, illustrating the velocity distribution between channels with stable bubbles. The disturbance level generated within the range of bubble affects the surrounding fluid differently depending on the bubble size, with larger bubbles primarily exhibiting perturbations along the horizontal direction. The velocity in the distribution area of the gas phase was much greater than the liquid phase and the maximum existed on the center line for a single slug bubble. The wake area exhibits extensive high-velocity zones crucial for scouring the membrane surface. The maximum velocity of 20-mL bubbles generated under a bubble stable state was obtained through post-processing, as shown in Fig. S4b, with an instantaneous peak velocity

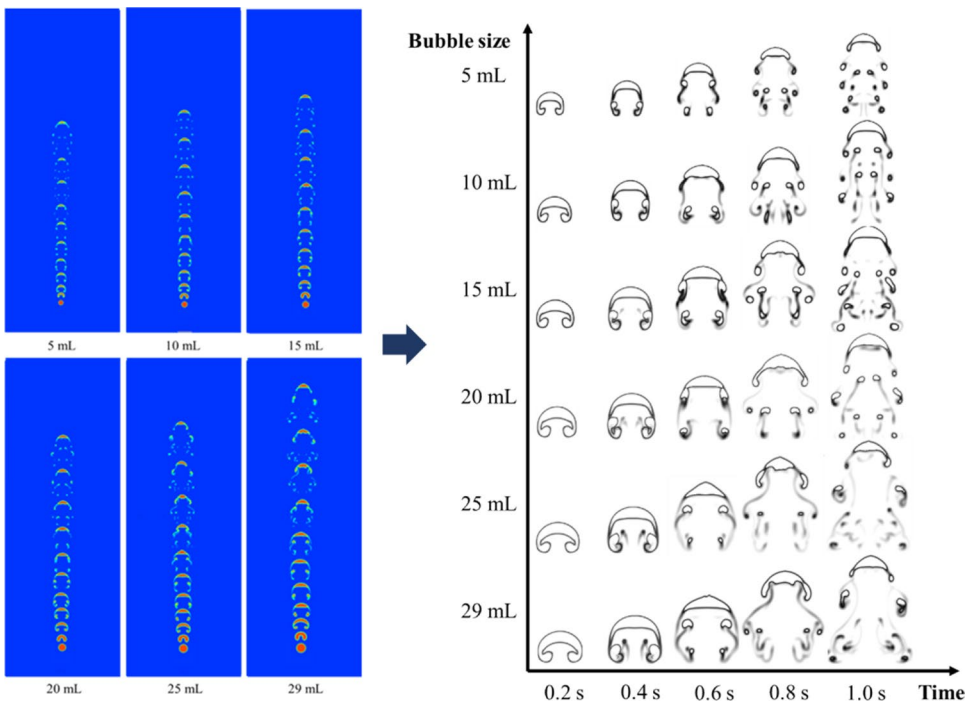

Fig. 2 Bubble evolution comparison of different sizes from 0.0 to 1.0 s

of 0.63 m/s at the local system level. The greater level of disturbance is induced by higher velocities, and the heightened intensity of disturbance is attributed to the triggered high velocities. The results revealed that a critical bubble size was necessary for a good value in running membrane modules, which needed further verification.

The relative frequency distribution of different intervals in Fig. 3 provided a further quantified insight into the velocity distribution. The slug bubbles of various sizes formed during aeration in the membrane system predominantly exhibit velocities concentrated in the low range (< 0.1 m/s). As the bubble size increased, the relative frequency of higher velocities within the flow region significantly rose. A peak value of 20.59% was observed at a 20-mL bubble size, corresponding to the velocity range between 0.1 and 0.6 m/s. Moreover, with the further increase in velocity, the disparity in relative frequency between the 20-mL bubble and other sizes diminished, resulting in sustained highest frequencies within the 0.25 to 0.6 m/s range (1.23%, 1.40%, 1.16%, 1.02%, 0.83%, 0.23%, and 0.02%). As shown in Fig. 4, the membrane surface region demonstrated a conspicuous concentration of high-velocity zones in both the gas slug and wake regions along the vertical direction. Under the influence of scouring and perturbation caused by the 20-mL bubble, a maximum velocity of 0.584 m/s is observed. The different-sized slug bubbles manifest similar trends in velocity variation along the vertical direction of the membrane surface. With an increasing bubble size, the velocity values expanded overall, and the numerical fluctuations exhibited an upward shift. The peak velocities generated under the 20-mL condition exceed those of other bubble sizes. Therefore, the aeration efficiency was maximized when employing a 20-mL bubble size.

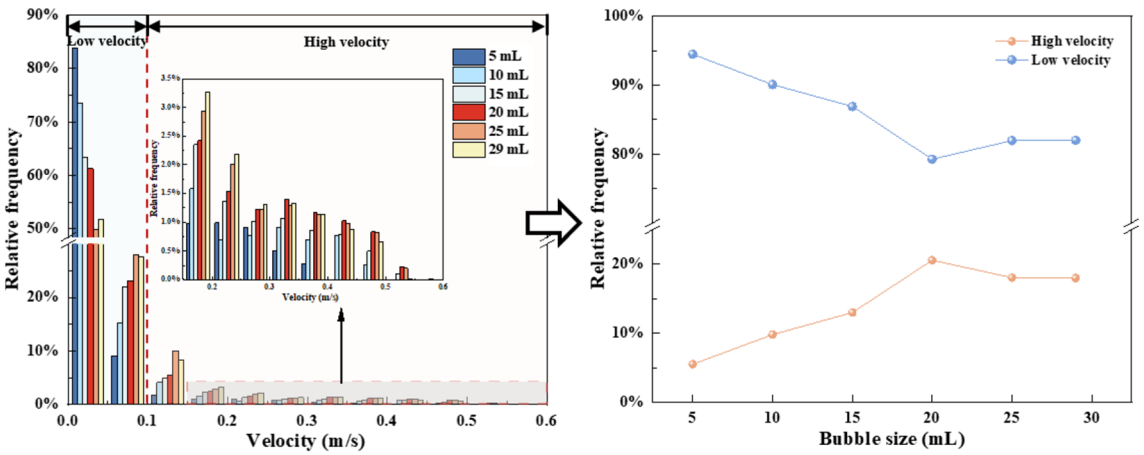

Fig. 3 Relative frequency distribution of different intervals in the flow velocity range

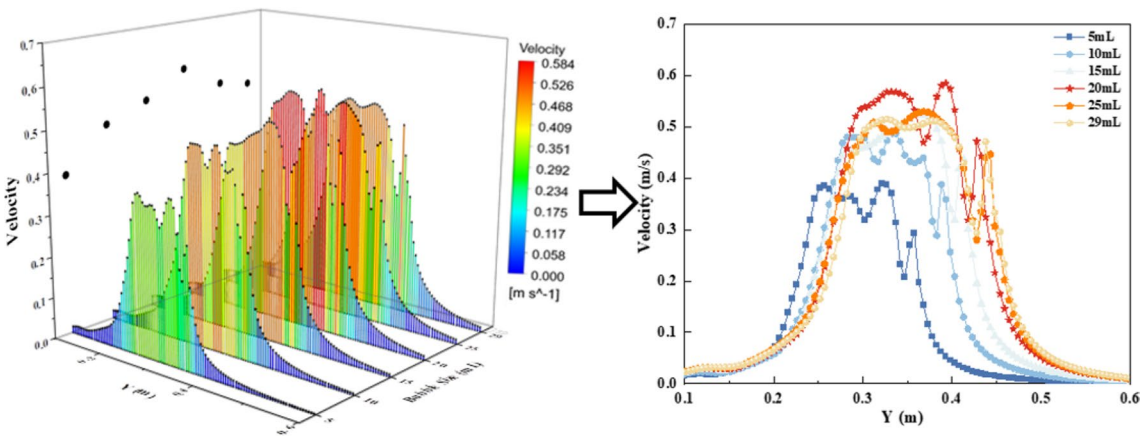

Fig. 4 Spatial distribution and maximum values of mean flow velocity along the height direction in the membrane surface area

Turbulent intensity

The turbulent intensity generated by slug bubbles significantly influences the flow characteristics in the wake region, as illustrated in Fig. 5. The concentration of turbulent energy was observed mainly in the gas slug region and the wake region. The peak values of 6.38%, 6.35%, and 5.99% were recorded under the specific condition of a 20-mL bubble size, surpassing the values observed for other bubble sizes. This highlights the notable impact of bubble size on the overall distribution of turbulent intensity. Furthermore, an analysis of the vertical distribution of turbulent intensity revealed an increasing trend near the wall as the bubble size increased. The turbulent intensity reached a maximum value of 16.57% under the 20-mL conditions associated with a 20-mL bubble size.. The turbulence intensity distribution map (Fig.S5) revealed that the leading region of the slug bubble corresponds to high turbulence, indicating low flow velocity. The interaction between the liquid–gas interface at the nose region of the slug bubble and the descending film results in the amplification of turbulent phenomena. This is attributed to the generation of shear forces and vortices, leading to enhanced turbulent intensity. Moreover, the lower flow velocities in the nose region, resulting from the trapping of liquid ahead of the bubble, contributed to the intricacy of the flow and further augmented the turbulent effects. These findings provided valuable insights into the intricate relationship between bubble size and turbulent intensity, shedding comprehensive light on the flow dynamics associated with slug bubbles. The enhanced understanding of these phenomena had implications for optimizing and designing various engineering processes involving multiphase flows.

The surrounding fluid was also prone to a propensity for liquid circulation following disturbance by bubbles, which was closely related to the alteration of velocity vectors for slug bubble. The appearance of trailing vortexes also proved effective in mitigating particle deposition on the membrane surface (Shi et al. 2019). Therefore, the corresponding velocity vector and trailing vortex were analyzed (Fig. 6). The results unveiled an intricate velocity field beneath larger bubbles, characterized by recirculation zones dispersed on either side of the wake. The region gradually enlarged with the increasing bubble size. And the distribution of the Q value revealed that the center of the bubble wakes was the area dominated by strain rates, which corresponded to the area of negative numbers. The loopback region gradually became significant and the range expanded as the bubble size increased. However, as the bubble size reached 20 mL, the vorticity tensor inside the bubble increased significantly. The vortex shedding inside the bubble was accompanied by bubble deformation, resulting in significant asymmetric deformation, which is consistent with the law of bubble evolution. Therefore, the largest turbulence level in the surrounding fluid was caused by the slug bubble at 20 mL. This is corroborated by the observed variation in the vortex intensity index, as depicted in Figure S6.

The effect of bubble size on shear stress

Shear stress distribution

The distribution of shear stress on the entire membrane surface with the bubble under a steady state is described in Fig. 7a. The coverage width of bubble-induced shear stress was associated with increased bubble size and more intensity in the wake region. The peaks were observed in the wake region as strongly dominant for a bubble size from 20 to 29 mL. Generally, with increasing bubble size, the phenomenon that the shear stress effect evoked by the wake region was much stronger than the region of the liquid film became more evident. Within the wake region, the distribution of shear stress was found to be intricate, encompassing areas with lower values, indicating rapid fluctuations in shear stress

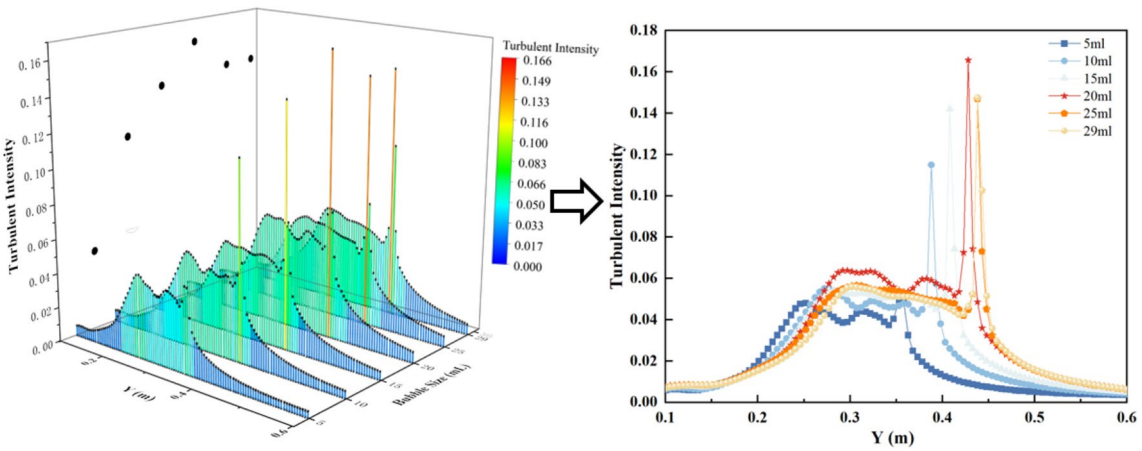

Fig. 5 Spatial distribution and maximum values of average turbulent intensity along the height direction in the membrane surface region

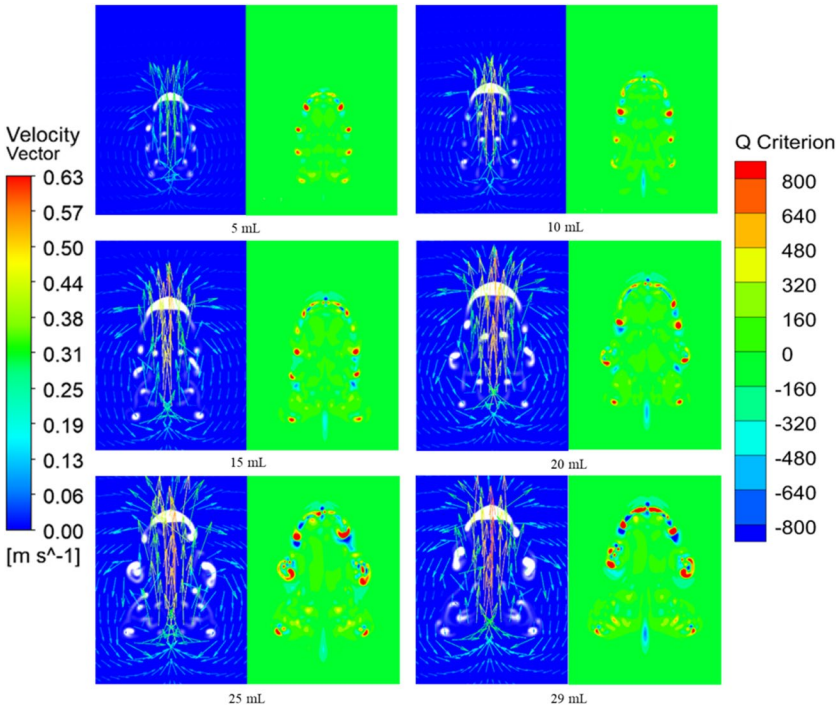

Fig. 6 The contour map of the velocity vector and the Q value distribution for each bubble size

levels. As shown in Fig. S7, the maximum shear stress was gradually increased from 1.18 to 1.71 Pa with the bubble size increased from 5 to 20 mL and peaked at 1.82 Pa; when the bubble size further raised to 29 mL, the max shear stress was gradually decreased. This result implied the 20-mL bubble might have the most substantial scouring effect, which matched the findings of the velocity in Fig. S4b.

The empirical "three-zone" model (Ghosh and Cui 1999) divides the membrane cross-section in the vicinity of the gas segment plug into three distinct zones as shown in Fig. 7a, including falling film, air slug, and wake region. The different regions of the slug bubbles were divided into segments starting from the corresponding position of the bubble nose at the initial point of 0 mm. Figure 7b shows the alteration in shear stress along the centerline, which is the red line shown in Fig. 4a. The overall variance in shear stress could be separated into three parts within the corresponding region. In the falling film region, an initial shear stress value at the bubble nose, which decreased approximately linearly to near zero. In the region of air slug, the shear stress gradually increased until reached a local maximum, which was 0.75 Pa, 0.97 Pa, 1.06 Pa, 1.17 Pa, 1.11 Pa, and 1.15 Pa for bubble sizes of 5 mL, 10 mL, 15 mL, 20 mL, 25 mL, and 29 mL, respectively. In the wake covering a larger area, culminating in multiple peak values before dropping to nearly zero, and the rapid fluctuation of shear stress in the wake was proved. Furthermore, the shear stress peaks induced by the wake of 20 mL bubbles were higher than those of other bubble sizes, with values of 1.47 Pa, 1.67 Pa, and 1.73 Pa. Therefore, the maximum shear stress effect was achieved in the wake region of the 20-mL bubble.

Probability of membrane fouling

As shown in Fig. 8a, the probability distribution of membrane fouling in the entire region of the membrane is obtained based on the calculated E value, which is derived from particle force analysis. The central region of the membrane surface, where the bubbles were positioned, exhibited predominantly low membrane fouling ($E < 0.5$). However, the edges of the corner region were more susceptible to contaminant deposition. The low fouling region gradually expanded with an increase in the size of the slug bubbles. Notably, at the 20-mL bubble size, the probability distribution of membrane fouling at the edges of the corner region appeared as the lightest color, indicating the lowest E value.

The analysis reveals from Fig. 8b indicates that the mean values of membrane fouling probability for bubble sizes ranging from 5 to 29 mL are 0.51, 0.40, 0.34, 0.26, 0.28, and 0.30, respectively. The scouring effect of 20-mL slug flow results in a maximum proportion of 48.17% for the low fouling probability region, while the minimum proportion for the high fouling probability region is 51.833%. The findings highlight the efficacy of slug flows with a 20-mL bubble size in reducing fouling risks.

Experimental results

TMP and fouling rate

As shown in Fig. 9, the measured transmembrane pressure (TMP) in all MBR systems underwent changes during the

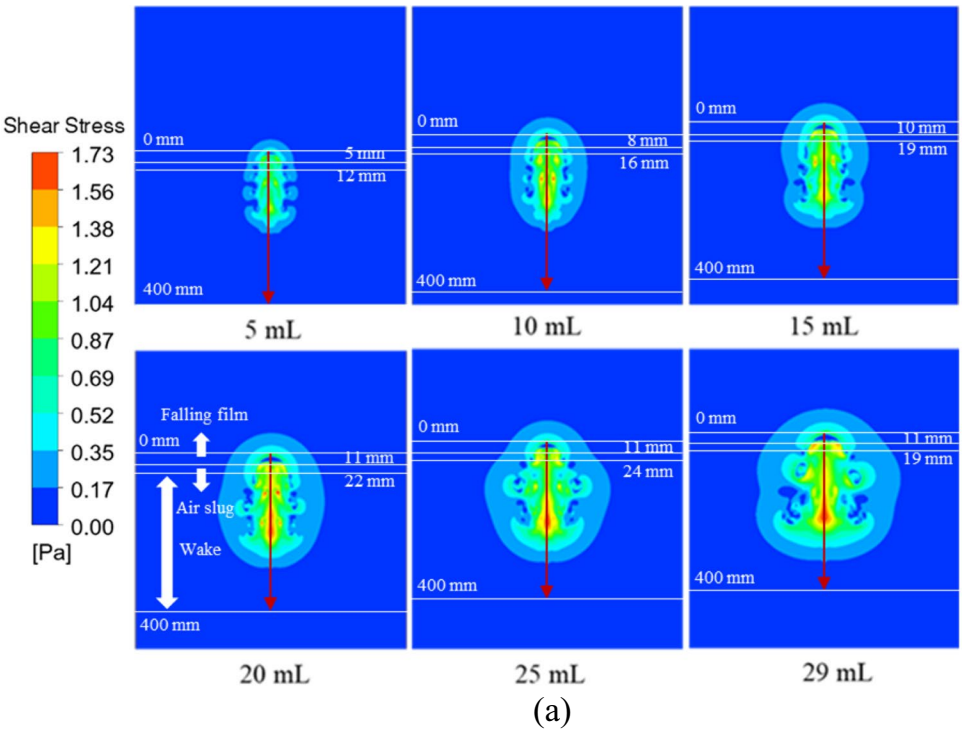

(a)

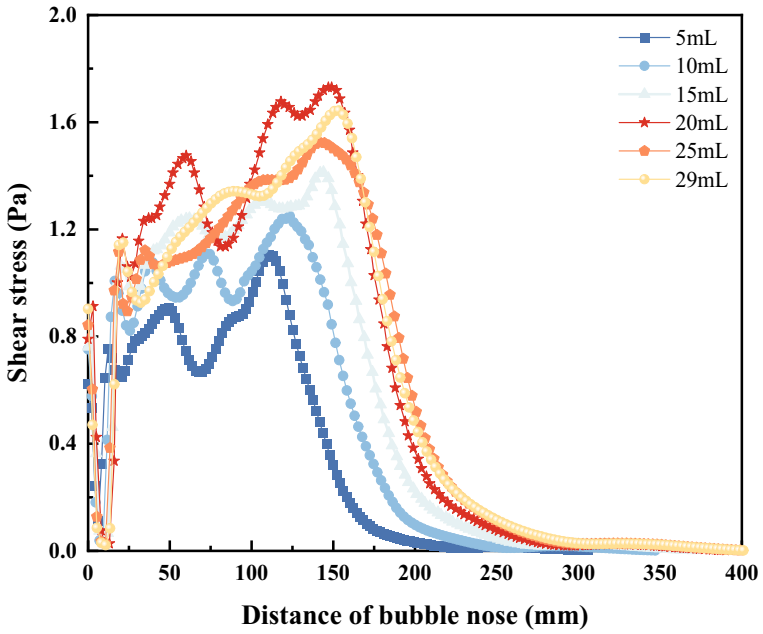

(b)

Fig. 7 Variation of (**a**) shear stress distribution and (**b**) the spatial fluctuation of shear stress along the center line of the membrane with different bubble sizes

operational cycle due to membrane fouling. The TMP registered a negative pressure with an initial value of approximately – 10 kPa, indicating a moderately appropriate filtration pressure. The consistent decrease in TMP over time, signifying an upward trend in absolute values within the context of negative TMP values. The 20-mL bubble demonstrated the least extent of membrane fouling, evident in the ongoing minimal absolute values of TMP and a continuous reduction in the disparity between influent and filtration pressures throughout the entire cyclic process. This finding highlights the remarkable performance of the 20-mL bubble in mitigating membrane fouling when compared to other bubble sizes under aeration conditions. This was consistent with the simulation results of membrane fouling probability.

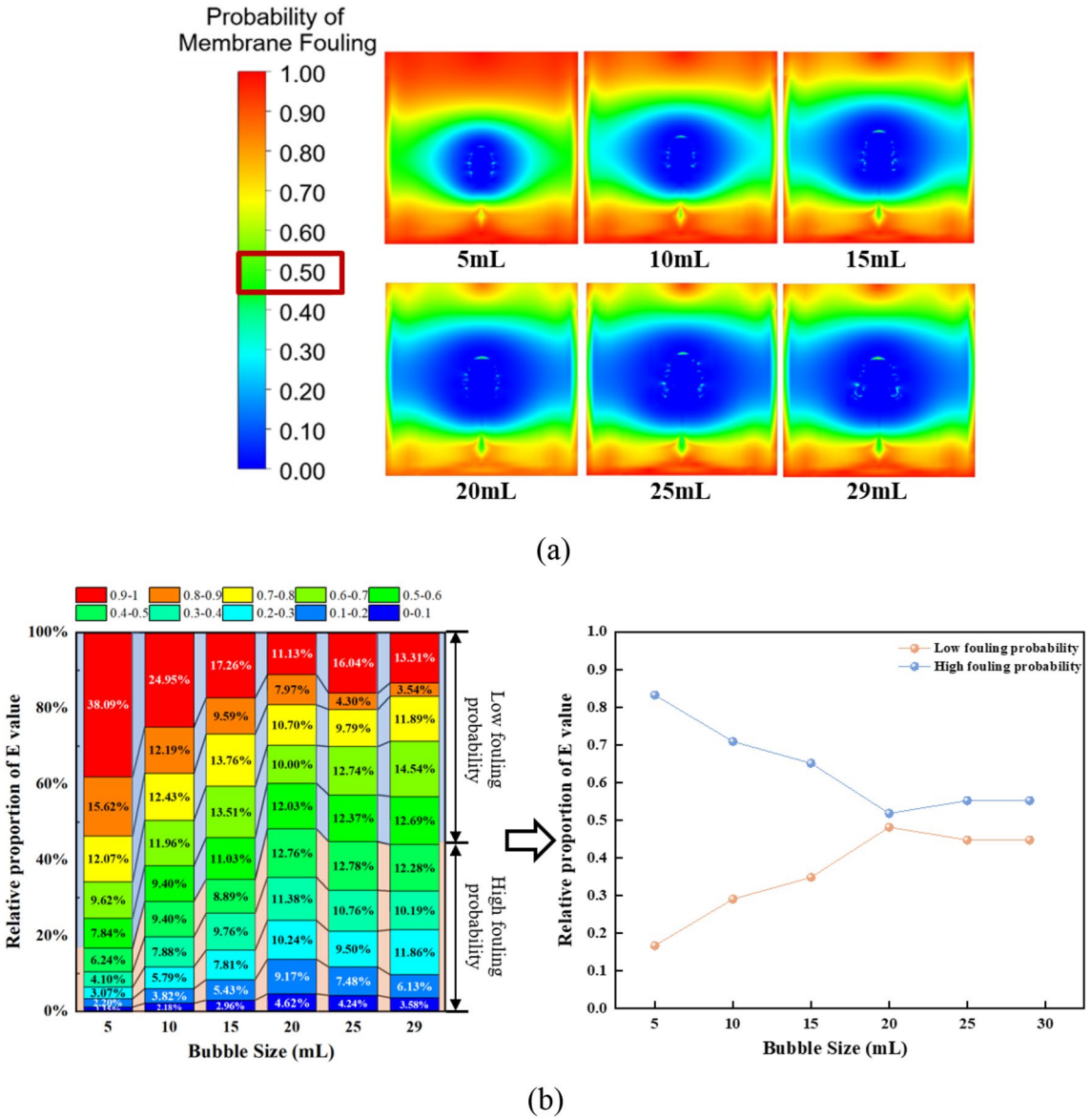

Fig. 8 **a** The distribution of probability of membrane fouling and (**b**) the relative proportion of *E* value with different bubble sizes

The further analysis was conducted to investigate the main factors that caused the fouling rate of the membrane.

The 20-mL slug bubble exhibited the slowest fouling rate compared to the other sizes studied as shown in Fig.S8 and played a significant role in mitigating membrane fouling in the MBR system. Several factors contributed to the lower fouling propensity and slower fouling rate observed with the 20-mL bubble. Firstly, the size and shape of the slug bubble facilitated efficient scouring and cleaning actions on the membrane surface, thereby restricting the accumulation of foulants. Additionally, the hydrodynamic characteristics of the 20-mL slug bubble, including its velocity and interaction with the membrane surface reduced fouling propensity.

Terminal velocity of bubbles

The terminal velocity data of the slug bubble was calculated for the steady-state head bubble at the corresponding ascending distance after analyzing the captured images with image processing software. The results revealed that the terminal velocities of slug bubbles with volumes of 5 mL, 10 mL, 15 mL, 20 mL, 25 mL, and 29 mL were determined as 0.0137 m/s, 0.0214 m/s, 0.0263 m/s, 0.0309 m/s, 0.0285 m/s, and 0.281 m/s, respectively. The obtained data demonstrate that the 20-mL slug bubble exhibited the highest terminal velocity among the different volumes investigated. The observation highlights the consistency between the advantage of utilizing 20-mL bubbles to achieve maximum disturbance in membrane bioreactor (MBR)

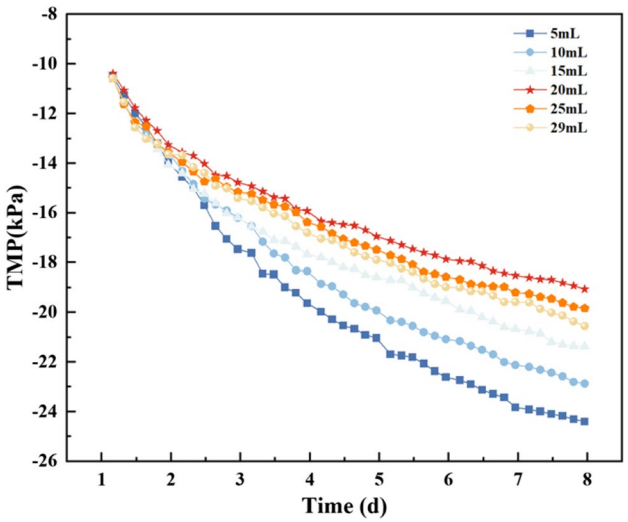

Fig. 9 Transmembrane pressure variation during MBR operation cycle under aeration conditions with different slug bubble sizes

systems and the simulated results. The increased terminal velocity indicates a shorter residence time of bubbles in the liquid phase, facilitating improved contact and enhanced mass transfer between pollutants and the membrane surface. Moreover, the faster rise of the 20-mL slug bubble, compared to smaller sizes, suggests lower energy requirements for bubble generation and maintenance. This attribute aligns with the objective of energy optimization within MBR systems. The relatively larger size of the 20-mL bubble minimizes interference and collisions between bubbles, contributing to operational stability.

SEM

The analysis of SEM images (Fig. 10) revealed the influence of different aeration conditions on membrane surface fouling and pore blockage. The original membrane pores were dense and nearly uniform in size. The utilization of a small bubble size of 5 mL, resulted in a marked escalation of membrane surface fouling, accompanied by pronounced

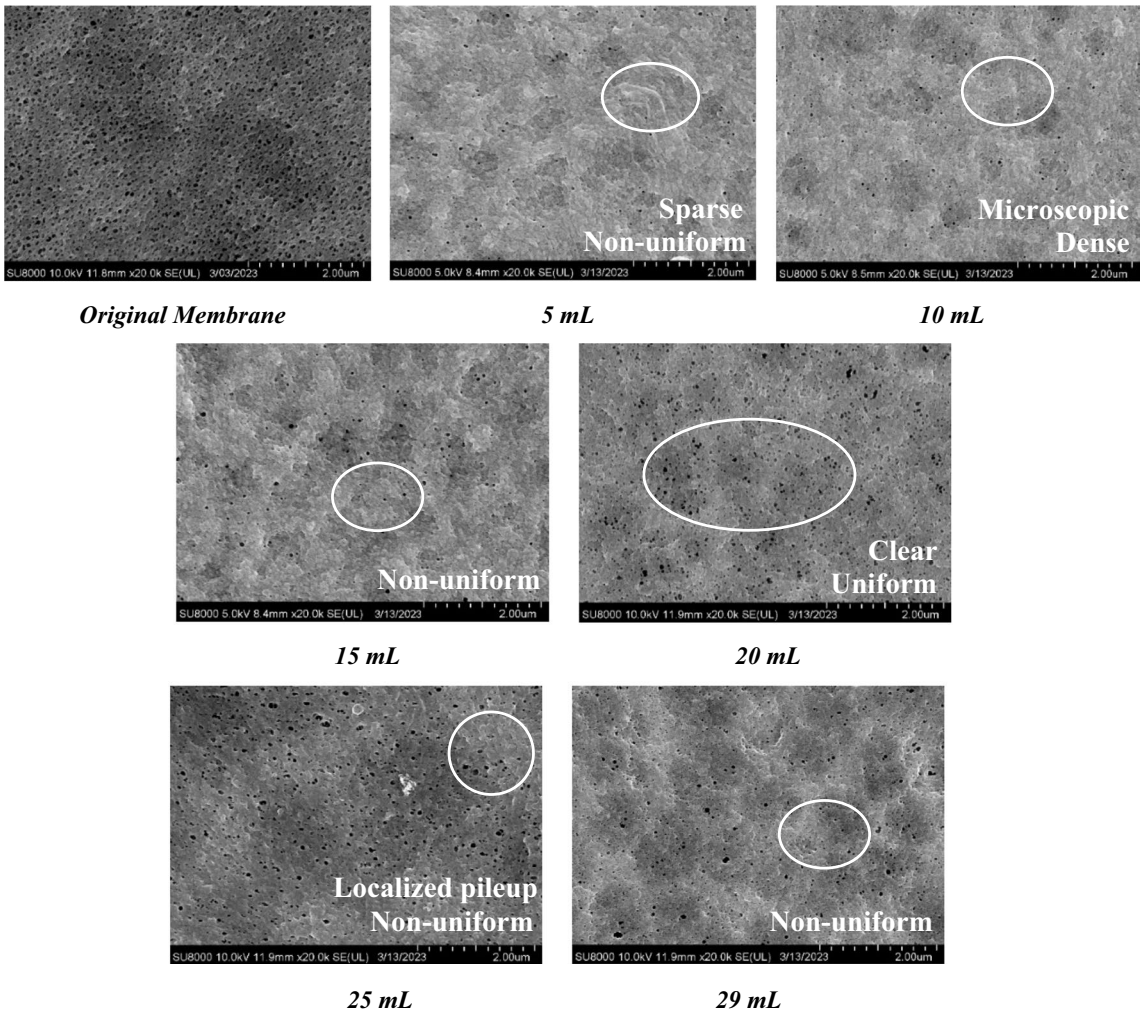

Fig. 10 SEM images of the original membranes and membrane of aeration conditions with different slug bubble sizes

pore blockage. As the bubble size increased to 10 mL and 15 mL, the membrane pores gradually became more visible, resulting in a gradual reduction of surface fouling.

Additionally, a closer analysis revealed differences in the extent and distribution of fouling on the membrane surface between the 25- and 29-mL bubble sizes. At the 20-mL bubble size, the membrane exhibited clear pores and a relatively uniform fouling pattern with moderate coverage of contaminants. In contrast, with the 25-mL bubble size, although comparable to the 20-mL bubble size, the distribution of contaminants appeared more uniform. Certain regions on the membrane surface showed lower fouling density, while other areas exhibited higher concentrations of membrane fouling. At a bubble size of 29 mL, the fouling layer became dense again, and pore blockage reappeared. This suggested that a bubble size of 20 mL represented the optimal condition with clear and uniformly dense membrane pores. This finding aligned well with the probability distribution of membrane fouling and could be considered the most favorable bubble size.

Conclusions

CFD simulations were conducted on rising single slug bubbles in a flat-sheet ultrafiltration MBR, combining experimental results from practical applications to optimize bubble size. This study mainly includes as follows:

(1) The asymmetric deformation of a bubble affected the acceleration of surrounding fluid disturbances caused by the bubble evolution. The bubbles modeled were found to have a spherical cap form, with three main steps in the bubble evolution process. The asymmetric deformation of a bubble larger than 20 mL became progressively significant as the bubble size increased.
(2) The largest level of disturbances in the surrounding fluid was induced by the 20-mL slug bubble. The bubble generated an instantaneous peak velocity of 0.63 m/s at the local system level and an ascending terminal velocity of 0.0309 m/s, conducive to bubble scouring. The turbulence intensity and vortex index produced by this size of the bubble were higher compared to other sizes.
(3) The 20-mL bubble induced the most pronounced shear effect on the membrane surface, leading to the most effective reduction in membrane contamination. The wake region as the primary contributor to significant shear stress. The scouring effect of the 20-mL slug flow resulted in a peak proportion of 48.17% within the low fouling probability region, effectively reducing membrane fouling.
(4) The 20 mL was the optimal bubble size for ultra-thin flat sheet MBR in practical applications. This bubble size led to the lowest degree of membrane fouling throughout the entire cyclic process during actual operation. The aeration conditions of the 20-mL bubble size consistently exhibited lower absolute values of TMP and the lowest fouling rate compared to other bubble sizes.

Supplementary Information The online version contains supplementary material available at https://doi.org/10.1007/s11356-024-32195-3.

Acknowledgements The authors are also grateful to the reviewers and the editor for their helpful comments.

Author contribution XW: design of the work and drafting the work. LY and JC: the acquisition and analysis. SD: substantively revised it. FX: reviewing it critically for important intellectual content.

Funding The authors gratefully acknowledge support from the National Natural Science Foundation of China (NSFC: 5203003).

Data availability All data generated or analyzed during this study are included in this published article (and its supplementary information files).

Declarations

Ethical approval Not applicable.

Consent to participate Not applicable.

Consent for publication Not applicable.

Competing interest The authors declare no competing interests.

References

Brackbill JU, Kothe DB, Zemach C (1992) A continuum method for modeling surface tension. J Comput Phys 100:335–354
Clift R, Grace JR, Weber ME (1979) Bubbles, drops, and particles. Dry Technol 11:263–264
Du X, Liu X, Wang Y, Radaei E, Lian B, Leslie G, Li G, Liang H (2017) Particle deposition on flat sheet membranes under bubbly and slug flow aeration in coagulation-microfiltration process: effects of particle characteristic and shear stress. J Membr Sci 541:668–676
Feng X, Yang C, Mao Z-S, Lu J, Tryggvason G (2019) Bubble induced turbulence model improved by direct numerical simulation of bubbly flow. Chem Eng J 377:120001
Gao Z, Wang J, Wang J, Mao Y, Wei Y (2019) Analysis of the effect of vortex on the flow field of a cylindrical cyclone separator. Sep Purif Technol 211:438–447
Ghosh R, Cui ZF (1999) Mass transfer in gas-sparged ultrafiltration: upward slug flow in tubular membranes. J Membr Sci 162:91–102
Golrokh Sani A, Najafi H, Azimi SS (2021) CFD simulation of air-sparged slug flow in the flat-sheet membrane: a concentration polarization study. Sep Purif Technol 270:118816
Grace JR, Wairegi T, Nguyen TH (1976) Shapes and velocities of single drops and bubbles moving freely through immiscible liquids. Transact Institut Chem Eng 54:167–173
Grace JR (1973) Shapes and velocities of bubbles rising in infinite liquids. Transact Institut Chem Eng 51:116–120

Grace JR (1983) Hydrodynamics of liquid drops in immiscible liquids. In: Cheremisinoff NP, Gupta R (eds) Handbook of fluids in motion, Chapter 38. Ann Arbor Science, The Butter-worth Group, Ann Arbor, MI

Gumulya M, Utikar RP, Pareek VK, Evans GM, Joshi JB (2021) Dynamics of bubbles rising in pseudo-2D bubble column: effect of confinement and inertia. Chem Eng J 405:126615

Hashisho J, El-Fadel M, Al-Hindi M, Salam D, Alameddine I (2016) Hollow fiber vs. flat sheet MBR for the treatment of high strength stabilized landfill leachate. Waste Manage 55:249–256

He L, Wang Y, Zhou T, Zhao Y (2020) Enhanced ammonia resource recovery from wastewater using a novel flat sheet gas-permeable membrane. Chem Eng J 400:125338

Hirt CW, Nichols BD (1981) Volume of fluid (VOF) method for the dynamics of free boundaries. J Comput Phys 39:201–225

Kaya R, Deveci G, Turken T, Sengur R, Guclu S, Koseoglu-Imer DY, Koyuncu I (2014) Analysis of wall shear stress on the outside-in type hollow fiber membrane modules by CFD simulation. Desalination 351:109–119

Kovalchuk N, Starov V, Langston P, Hilal N, Zhdanov V (2008) Colloidal dynamics: influence of diffusion, inertia and colloidal forces on cluster formation. J Colloid Interface Sci 325:377–385

Lan Y, Groenen-Serrano K, Coetsier C, Causserand C (2017) Fouling control using critical, threshold and limiting fluxes concepts for cross-flow NF of a complex matrix: membrane BioReactor effluent. J Membr Sci 524:288–298

Liu X, Ji C, Xu X, Xu D, Williams JJR (2017) Distribution characteristics of inertial sediment particles in the turbulent boundary layer of an open channel flow determined using Voronoï analysis. Int J Sedim Res 32:401–409

Liu M, Yang M, Chen M, Yu D, Zheng J, Chang J, Wang X, Ji C, Wei Y (2018) Numerical optimization of membrane module design and operation for a full-scale submerged MBR by computational fluid dynamics. Biores Technol 269:300–308

Liu L, Yan H, Ziegenhein T, Hessenkemper H, Li Q, Lucas D (2019) A systematic experimental study and dimensionless analysis of bubble plume oscillations in rectangular bubble columns. Chem Eng J 372:352–362

Liu J, Fu W, Yu X, Yang H, Zhao D, Wang Z, Wang L, Li X, Tang CY (2023) Relating critical and limiting fluxes to metastable and long-term stable fluxes in colloidal membrane filtration through collision-attachment theory. Water Res 238:120010

Meng F, Zhang S, Oh Y, Zhou Z, Shin H-S, Chae S-R (2017) Fouling in membrane bioreactors: an updated review. Water Res 114:151–180

Ndinisa NV, Fane AG, Wiley DE, Fletcher DF (2006) Fouling control in a submerged flat sheet membrane system: part II—Two-phase flow characterization and CFD simulations. Sep Sci Technol 41:1411–1445

Ngo SI, Lim Y-I, Kwon HM, Lee U-D (2023) Hydrodynamics of molten-metal bubble columns in the near-bubbling field using volume of fluid computational fluid dynamics. Chem Eng J 454:140073

Radaei E, Liu X, Tng KH, Wang Y, Trujillo FJ, Leslie G (2018) Insights on pulsed bubble control of membrane fouling: effect of bubble size and frequency. J Membr Sci 554:59–70

Ratkovich N, Chan CCV, Berube PR, Nopens I (2009) Experimental study and CFD modelling of a two-phase slug flow for an airlift tubular membrane. Chem Eng Sci 64:3576–3584

Shi W, Yang X, Sommerfeld M, Yang J, Cai X, Li G, Zong Y (2019) Modelling of mass transfer for gas-liquid two-phase flow in bubble column reactor with a bubble breakage model considering bubble-induced turbulence. Chem Eng J 371:470–485

Shih T-H, Liou WW, Shabbir A, Yang Z, Zhu J (1995) A new k-ϵ eddy viscosity model for high Reynolds number turbulent flows. Comput Fluids 24:227–238

Tripathi MK, Sahu KC, Govindarajan R (2015) Dynamics of an initially spherical bubble rising in quiescent liquid. Nat Commun 6:6268

Wang H, Brito-Parada PR (2021) Shape deformation and oscillation of particle-laden bubbles after pinch-off from a nozzle. Chem Eng J 412:127499

Wang Z, Ma J, Tang CY, Kimura K, Wang Q, Han X (2014) Membrane cleaning in membrane bioreactors: a review. J Membr Sci 468:276–307

Wang B, Zhang K, Field RW (2018) Optimization of aeration variables in a commercial large-scale flat-sheet MBR operated with slug bubbling. J Membr Sci 567:181–190

Wang J, Lv M, Huang Y, Huang L, Ying X, Xu Y, Shen D, Feng H, Zhang X (2021) Numerical simulation and optimization of a cold model of a flat membrane bioreactor air scouring for membrane fouling control. J Membr Sci 640:119814

Wang B, Zhang Y, Fang Y, Zhang K, Field RW (2022) Aeration pipe design for free bubbling hydrodynamic optimization of flat sheet MBRs. J Membr Sci 646:120222

Wei P, Zhang K, Gao W, Kong L, Field R (2013) CFD modeling of hydrodynamic characteristics of slug bubble flow in a flat sheet membrane bioreactor. J Membr Sci 445:15–24

Xiao K, Liang S, Wang X, Chen C, Huang X (2019) Current state and challenges of full-scale membrane bioreactor applications: a critical review. Biores Technol 271:473–481

Youngs D (1982) Numerical methods for fluid dynamics. Academic Press

Zhan J, Li Y, Wai WO, Hu W (2019) Comparison between the Q criterion and Rortex in the application of an instream structure. Phys Fluid 31:121701

Zhang K, Cui Z, Field RW (2009) Effect of bubble size and frequency on mass transfer in flat sheet MBR. J Membr Sci 332:30–37

Zhang K, Cui Z, Field RW (2019) Effect of bubble size and frequency on mass transfer in flat sheet MBR. J Membr Sci 332:30–37

Zhang W, Wang J, Li B, Yu K, Wang D, Yongphet P, Xu H, Yao J (2021) Experimental investigation on bubble coalescence regimes under non-uniform electric field. Chem Eng J 417:127982